

Peter H. Wilkins¹

Pennsylvania State University,
University Park, PA 16802
e-mail: phw13@psu.edu

Stephen P. Lynch

Pennsylvania State University,
University Park, PA 16802
e-mails: splynch@psu.edu;
spl11@psu.edu

Karen A. Thole

Pennsylvania State University,
University Park, PA 16802
e-mail: kthole@psu.edu

Tyler Vincent

Pratt & Whitney,
East Hartford, CT 06118
e-mail: tyler.vincent2@prattwhitney.com

San Quach

Pratt & Whitney,
East Hartford, CT 06118
e-mail: san.quach@prattwhitney.com

Eleanor Kaufman

Pratt & Whitney,
East Hartford, CT 06118
e-mail: eleanor.kaufman@prattwhitney.com

Experimental Investigation Into the Effect of a Ceramic Matrix Composite Surface on Film Cooling

Ceramic matrix composite (CMC) components enable high turbine entry temperatures, which can lead to improved efficiencies in gas turbines. Implementing film cooling over CMC components, similar to how it is employed for conventional metal components, can extend part life and push operating temperatures beyond the temperature capabilities of CMCs alone. However, CMCs have a unique surface topology that can influence film cooling performance. Often this topology takes the form of an irregular wavy pattern due to the weave of the fibers that make up the strengthening component of the composite. In this study, shaped 7–7 film cooling holes are embedded in a five-harness-satin weave pattern representative of a CMC, at two orientations of the pattern. Detailed adiabatic film effectiveness measurements are obtained in a wind tunnel using an infrared camera while near-wall flowfield measurements are obtained with a high-speed particle image velocimetry system. A range of blowing ratios between one and three are investigated at a density ratio of 1.5 and freestream turbulence intensities of 0.5% and 13%. Across the majority of the tested conditions, the CMC surfaces result in lower film cooling performance than a smooth surface. At a freestream turbulence intensity of 0.5%, the adiabatic film effectiveness is moderately insensitive to the blowing ratio for both weave orientations. The boundary layer over the CMC surfaces increases the mixing between the coolant and the mainstream through a combination of increased turbulence, reduced near-wall velocities, and a thicker boundary layer. [DOI: 10.1115/1.4055332]

Keyword: heat transfer and film cooling

Introduction

After many years of investigation and exploration, the use of ceramic matrix composites (CMCs) is becoming more prevalent in high-efficiency air and land-based turbines. The opportunity for improved performance in gas turbines and other high-temperature applications is derived by the high heat resistance and relatively lower density of CMCs compared to nickel alloys [1,2]. Using CMCs to replace components with lower allowable temperature enables higher operating temperatures thereby improving cycle efficiency. Alternatively, replacing highly cooled components with CMCs reduces the amount of required coolant air that is a penalty to efficiency. Reductions in weight also yield efficiency benefits for aircraft engines.

Although common for nickel superalloy material systems, film cooling over CMCs is subject to several unique challenges, namely distortion of the hole outlet shape, and a surface topology that has potentially significant variations in amplitude and length relative to the film cooling jet scale. Additionally, weave roughness is directional with each orientation having its own unique characteristics, resulting in local separations as observed by Wilkins et al. [3]. Understanding the impact that CMCs have on film cooling will be an important step in designing the next generation of gas turbines.

In this study, two different five-harness-satin (weave type) (5HS) CMC surfaces, one with its long-exposed tows parallel to the freestream and one with its long-exposed tows perpendicular to the freestream, are tested across a range of conditions. These test conditions

include blowing ratios between 1.0 and 3.0 and freestream turbulence intensity levels of $Tu_{\infty} = 0.5\%$ and $Tu_{\infty} = 13\%$. The performance of the CMC surfaces is then compared to measurements taken over a smooth surface by Schroeder and Thole [4,5], highlighting the differences between CMC and smooth surfaces under different turbulence intensities.

Background

CMCs by the nature of their composite construction have unique material characteristics relative to conventional turbine materials. An increasing number of studies have examined the impact of anisotropic thermal properties in CMCs, although most of these studies have focused on smooth internal and external surfaces. One numerical study investigating the impact of the anisotropy on film cooling performance by Bryant and Rutledge [6] found that the standard orientation of CMCs with plies parallel to the flow over the surface is the least effective orientation for cooling, with limited conduction effects due to the disjointed conduction paths through the material. A similar numerical study was conducted by Tu et al. [7], who found that orienting the plane of a ply perpendicular to the oncoming flow results in improved cooling performance due to augmented conduction effects through the surface. A subsequent study by Tu et al. [8] experimentally investigated the impact of anisotropic thermal conduction of CMCs with film cooling, reinforcing the finding from their previous study.

Prokein et al. [9] investigated the potential for natural cracks within a porous carbon/carbon CMC to produce transpiration cooling at supersonic gas path conditions. From this study, Prokein et al. determined that using the internal cracks of CMCs as coolant channels is an effective way at cooling both the

¹Corresponding author.

Contributed by the International Gas Turbine Institute (IGTI) of ASME for publication in the JOURNAL OF TURBOMACHINERY. Manuscript received July 13, 2022; final manuscript received August 12, 2022; published online September 15, 2022. Tech. Editor: David G. Bogard.

transpired surface and downstream of the transpired surface. Zhong and Brown [10] investigated effusion cooling over SiC/SiC and Ox/Ox CMC components using test articles that were composed of CMC weaves with cylindrical holes drilled in multiple rows across the surface. Across the range of blowing ratios tested they found that increasing the blowing ratio results in improved cooling performance with improvements in performance diminishing at higher blowing ratios.

It is unclear yet whether the more regular surface topography of a CMC could be analogous to random roughness effects. One of the first studies to investigate the impact of external surface roughness on film cooling performance was conducted by Goldstein et al. [11] with cylindrical holes. Goldstein et al. found that at low blowing ratios the addition of roughness leads to a reduction in film cooling performance. However, once reaching a blowing ratio where jet detachment is expected, the rough surfaces outperformed the smooth surface at the same blowing ratio. The likely cause of this relative increase is the increased mixing over the rough surface bringing some of the detached coolants back to the wall.

Building on the work done by Goldstein et al. [11], Barlow and Kim [12] investigated the impact of roughness using modified cones at a freestream turbulence level of $Tu_\infty = 8.5\%$ for cylindrical film holes at a 30 deg surface angle. Barlow and Kim found that across the range of blowing ratios tested the surface roughness resulted in reduced cooling on an area-averaged basis relative to a smooth surface. This trend contradicts the earlier results by Goldstein et al., which Barlow and Kim attributed to the different oncoming boundary layer thickness and influence of freestream turbulence.

Investigating the impact of roughness at higher density ratios more similar to actual gas turbine conditions, Schmidt et al. [13] used a density ratio (DR) of two over conical roughness elements with cylindrical holes. The conical roughness elements were sized to generate an equivalent sand grain roughness as determined by Bogard et al. using in-service turbine components [14]. At a freestream turbulence level of 0.3%, Schmidt et al. found that similar to Barlow and Kim [12], surface roughness resulted in an increase in lateral spreading and a drop in centerline effectiveness. Additionally, Schmidt et al. also found an increase in relative cooling effectiveness for rough surfaces when compared to a smooth surface at higher blowing ratios at far downstream locations, similar to observations made by both Goldstein et al. [11] and Barlow and Kim [12].

Expanding upon Schmidt et al. [13], Schmidt and Bogard [15] investigated the impact of adding high freestream turbulence equal to $Tu_\infty = 17\%$ to the geometries defined in Schmidt et al. Compared to the $Tu_\infty = 0.3\%$ case, the $Tu_\infty = 17\%$ case resulted in a reduction of cooling effectiveness across the entire length tested. But when comparing the rough $Tu_\infty = 17\%$ case to the smooth $Tu_\infty = 17\%$ case, the rough surface outperformed the smooth surface and persisted further downstream. Thus, interactions of wall roughness and freestream turbulence may be complicated for film cooling.

Other investigations into the impact of high freestream turbulence on film cooling have been primarily conducted on smooth surfaces. One of these was conducted by Bons et al. [16] who found that elevated turbulence reduces the cooling effectiveness at the hole exit, but leads to improved cooling effectiveness at locations further downstream of the cooling hole. Kohli and Bogard [17] investigated the underlying physics responsible for this behavior and found that at elevated freestream turbulence levels turbulence generated by the shear layer is quickly replaced by the freestream turbulence as the dominant mode of turbulence. Larger scale turbulence leads to increased mixing that, at high blowing ratios, leads to more coolant near the wall far downstream of the cooling holes. The reattachment of coolant at high blowing ratios with elevated freestream turbulence was also observed by Schroeder and Thole [5] for shaped holes.

Recent work by Wilkins et al. [3] investigated the impact of CMC weave patterns on heat transfer augmentation and near-wall boundary layer behavior. In this study, Wilkins et al. found that at the

leading edge of a tow transition a region of stagnated flow was present that led to elevated heat transfer, while on the trailing edge of a tow transition the downward slope and rear-facing step created a region of separated flow that produced a region of reduced heat transfer. In a computational study by Wilkins et al. [18] the same behavior over tow transitions was observed and the behavior of film cooling over CMC weaves was investigated. For film cooling, it was found that the local features of the weave pattern have the potential to cause large local variations of cooling along the surface.

Many of the investigations into film cooling over CMCs have focused on effusion/transpiration cooling or how the anisotropic material properties of CMCs impact cooling performance, whereas much of the rough surface film cooling literature has focused on the impact of small roughness elements consistent with the scale of deposition/fouling. This study is the first to experimentally investigate the impact that macro-sized surface roughness features of CMC weave patterns have on film cooling and provide insight into the physical mechanisms.

Description of Surface Geometry

The CMC surface is simulated using a defined 5HS geometry originally described in Nemeth et al. [19]. This pattern was then modified by Wilkins et al. [3] to create a repeating unit cell (RUC) that is anisotropic and periodic along the x - z boundaries shown in Fig. 1. The long-exposed tows are labeled "A" tows and the shorter-exposed tows are labeled "B" tows. Two orientations of the geometry are considered: a 0 deg orientation where the "A" tows are aligned with the main flow direction and a 90 deg orientation where the "A" tows are perpendicular to the main flow direction. The base RUC 5HS weave pattern has a base tow width of $\lambda = 1.125$ mm and a base fabric thickness of $1/3 \lambda$.

The film cooling geometry that is tested is designed to match the computational model by Wilkins et al. [18]. This is done by combining the 5HS unit cell and the 7-7-7 shaped film cooling hole developed by Schroeder and Thole [4] into the scaled-up CMC surface. To match the scale of the hole tested by Schroeder and Thole, the 5HS weave pattern is scaled up 15.25 times with an assumed meter diameter of 0.51 mm at 1 \times scale for the 7-7-7 hole. The resulting surface has a $\lambda/D = 2.2$ and global surface roughness characteristics of $S_a = 0.57$ mm, $S_q = 0.70$ mm, and $S_z = 3.01$ mm. Then, the 7-7-7 hole with a scaled meter diameter of $D = 7.75$ mm is embedded within the CMC weave pattern, with the hole exit in the x - z plane matched to the mean height of the weave pattern as shown in Fig. 2. Each test plate is composed of

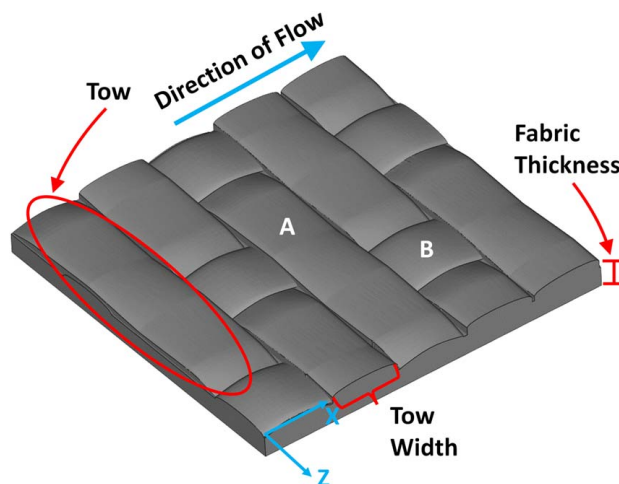


Fig. 1 5HS repetitive unit cell for 90 deg orientation

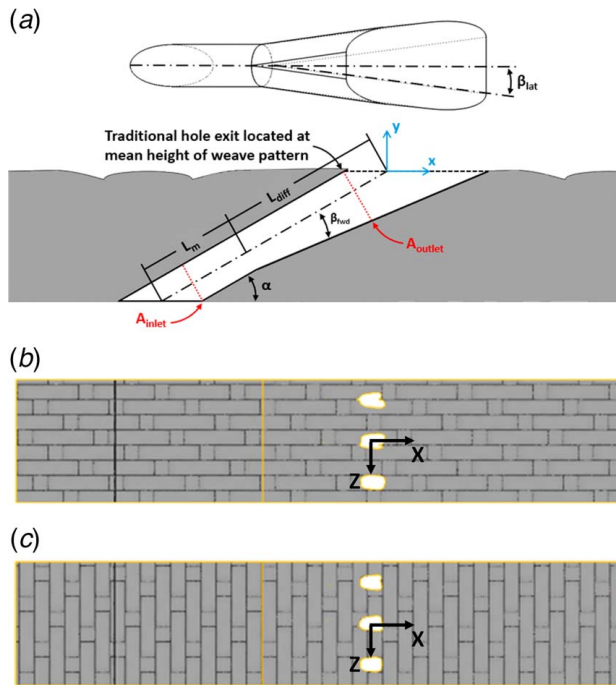


Fig. 2 (a) Cross-section of the 7-7 hole [4] embedded within a CMC surface, (b) 0 deg 5HS geometry, including flow conditioning region and hole outlet shapes, and (c) 90 deg 5HS geometry, including flow conditioning region and hole outlet shapes

five film cooling holes with a $P/D = 6$. This results in a film hole footprint that is unique for each hole in the CMC surface as a consequence of the local tow geometry at the hole exits. The presence of the outer holes is to provide a buffer between the tunnel outer wall and the coolant holes, improving the uniformity between the center three holes.

Experimental Facility and Methods

Film cooling experiments were performed in the closed-loop wind tunnel shown in Fig. 3. This wind tunnel has been used previously for film cooling studies by Eberly and Thole [20], Schroeder and Thole [4,5,21,22], and Haydt et al. [23–26]. The wind tunnel has a low-density mainstream loop at nearly room temperature, and a high-density secondary coolant loop cooled by liquid nitrogen with each loop possessing independent temperature control. The tunnel is positively pressurized with nitrogen to prevent moist air from flowing in and is dried using a desiccant vent dryer to reduce ambient moisture and prevent frost development. The mainstream is operated at 10 m/s and at a temperature of 328 K for both low and high turbulence levels. Freestream velocity is measured using a Pitot probe and freestream temperature is measured using thermocouples suspended from the top of the test section.

Freestream turbulence is generated using the same approach as Schroeder and Thole [5], where large vertical bars are located upstream at $x/b = -14$, where $b = 38$ mm is the bar diameter and x is defined according to the hole coordinate system shown in Fig. 2. The resulting turbulence levels at $x/D = -2$ are 0.5% and 13% for the two turbulence cases tested [5]. Upstream of the coolant holes is a boundary layer suction system enabling a fresh boundary layer to develop at the beginning of the test plate. To ensure a fully turbulent boundary layer a boundary layer trip 0.16D in height located at $x/D = -33$ is used.

Adiabatic Effectiveness Measurements. Adiabatic effectiveness film cooling measurements are taken in a similar manner to the method described in Schroeder and Thole [4], in that infrared thermography (IR) is used to measure surface temperatures on a foam surface. Unique to this study, a mold of the CMC surface is created using a large-scale 3D printed stereolithography material ($k = 0.208$ W/m K) with a $100\text{ }\mu\text{m}$ resolution. The film cooling holes with a 3.2 mm wall thickness are also made using this material, where the exit footprint of the hole is shaped to match the mold exactly where the hole meets up with it. A two-part expanding foam

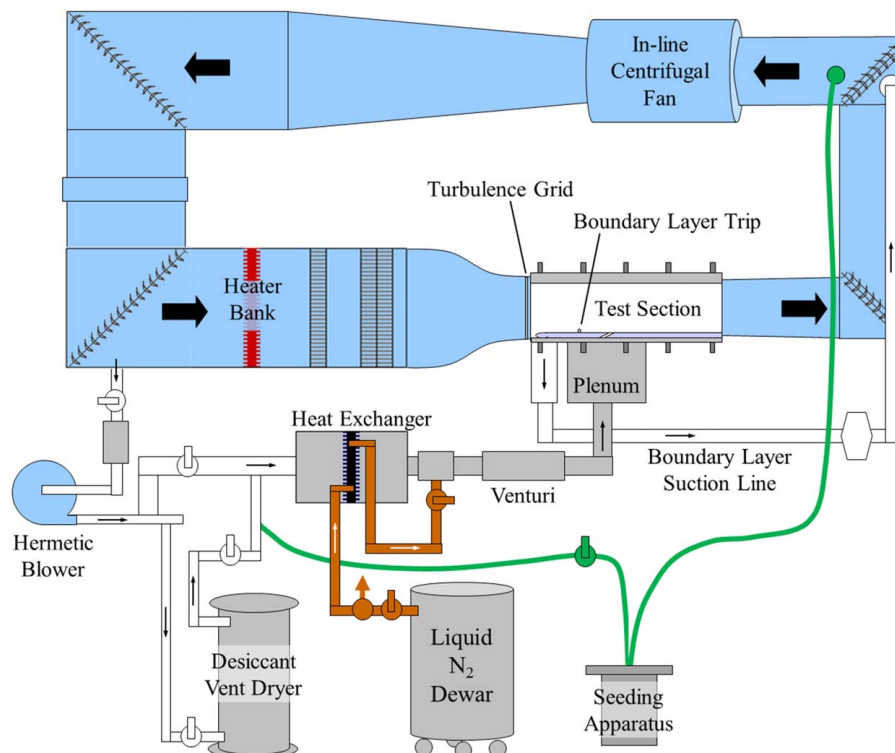


Fig. 3 Closed-loop wind tunnel facility used for the current study

with a thermal conductivity of 0.047 W/m K is cast into the mold and around the holes, such that the test plate contains the holes embedded in the foam and the top surface of the foam replicates the surface indicated in Fig. 2. The overall test plate thickness is approximately 25 mm to minimize conduction losses.

A FLIR SC620 infrared camera is used to measure the temperature of the foam surface downstream of the cooling holes. The infrared camera views the surface through a ZnSe window and is calibrated across the range of expected temperatures. IR calibration is done by placing temporary thermocouples directly downstream of the cooling holes, then once the mainstream of the tunnel is at operating temperature the secondary loop is slowly cooled. As the temperature over the thermocouples located at the hole exits decreases, a temperature calibration curve for that test case is created by matching the measured IR values to the measured thermocouple values. Once the calibration curve is created the thermocouples are removed from the surface. Once the appropriate density ratio and blowing ratio are achieved and are steady, the freestream temperature, plenum temperature, and calibrated local surface temperature from the camera are used to calculate local measured adiabatic effectiveness using Eq. (1):

$$\eta_{\text{measured}} = \frac{T_{\infty} - T_{\text{aw}}}{T_{\infty} - T_C} \quad (1)$$

The low thermal conductivity of the foam reduces but does not eliminate conduction loss; to account for this loss between the coolant plenum and the top surface of the foam, a one-dimensional thermal circuit analysis is performed. This is done by using the measured heat transfer coefficients on a CMC surface from Wilkins et al. [3], along with the freestream and plenum temperatures to calculate the conduction altered temperature on the test surface. Using the conduction-altered surface temperature (nondimensionalized as η_0), an adiabatic effectiveness excluding conduction effects is calculated as per Eq. (2) [27]

$$\eta = \frac{\eta_{\text{measured}} - \eta_0}{1 - \eta_0} \quad (2)$$

Flowfield Measurements. Flowfield measurements are taken along the center x - y plane shown in Fig. 4 using particle image velocimetry (PIV). To illuminate the particles, a dual-head Nd:YLF laser at 20 mJ per pulse with a 170 ns pulse width is used. Each laser head pulses at 3 kHz and the laser has a sheet thickness of 0.9 mm or 0.12 D . The freestream and the coolant loop are seeded with di-ethyl-hexyl-sebecat (DEHS) as tracer particles using an

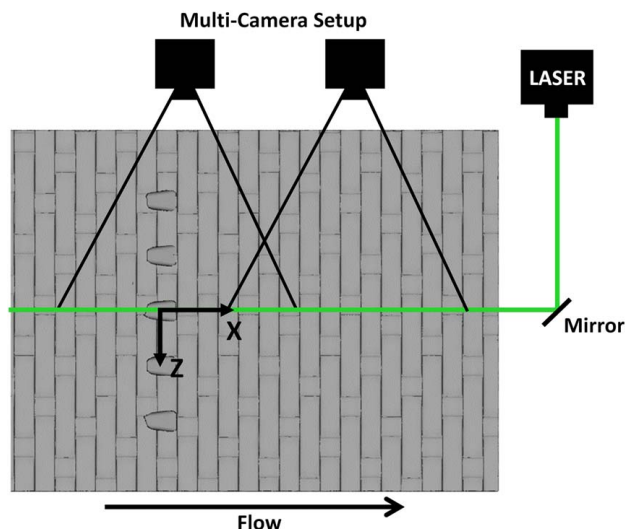


Fig. 4 Setup for cameras and laser for PIV measurements in the x - y plane at $z/D = 0$

aerosol generator that generates a mean particle diameter of 1 μm , resulting in a maximum Stokes number of 0.010 [5,28].

Two side-by-side complementary metal-oxide semiconductor (CMOS) cameras each with a resolution of 1280 \times 800 pixels are used to capture the particle image fields at a sampling rate of 3 kHz per image pair. Attached to each camera is a 105 mm lens with the aperture set to $f/4$. Stitching together images from each camera creates an image with the dimensions 20 D in the x direction and 6 D in the y direction. The time delay between the images in an image pair is 28 μs , resulting in a particle displacement of 8 pixels in the freestream. Image pairs are captured and post-processed using DaVis 10.1 [29].

Images are pre-processed to normalize the intensity and to remove reflections of the raw images. PIV calculations are done using side-by-side 2DPIV to calculate the flowfield across the two camera views to create one continuous vector image. Vectors are calculated using a multipass scheme with a 48 \times 48 pixel window that is reduced to 32 \times 32 pixels with 75% overlap that, given a spatial resolution of 13.2 pixels/mm, results in a window size of 0.31 \times 0.31 D . Vector post processing is used to remove vectors with a normalized correlation value below 0.25.

Uncertainty Analysis. Uncertainties are calculated using the methods described in Refs. [30,31] to calculate bias and precision uncertainty, where all precision uncertainties are calculated using a 95% confidence level. Density ratio was maintained throughout the range of tests and has an overall uncertainty of less than $\pm 1\%$. Uncertainty in the blowing ratio is higher with a maximum overall uncertainty of $\pm 5\%$ at $M = 1.5$. Adiabatic effectiveness is dominated by bias uncertainty, resulting in an overall uncertainty of $\delta\eta = \pm 0.025$. Flow field measurement uncertainty is calculated in DaVis using the method described by Wieneke [32], producing an average uncertainty in the velocity of $\pm 5\%$.

Results and Discussion

Adiabatic effectiveness and PIV measurements are taken across the 5HS weave pattern at two different orientations. Test conditions include a range of blowing ratios between 1.0 and 3.0 for adiabatic effectiveness measurements and two blowing ratios at 1.5 and 3.0 for PIV measurements. Over the CMC surfaces two freestream turbulence intensities are investigated, one low turbulence intensity at 0.5% and one high turbulence intensity at 13%. These measurements are compared to the adiabatic effectiveness and PIV measurements from Schroeder and Thole [4,5] for a smooth surface.

Low Freestream Turbulence Adiabatic Effectiveness. The adiabatic film effectiveness contours in Fig. 5 show the performance of the 7-7-7 film cooling hole at a freestream turbulence level of 0.5% and a blowing ratio of 1.5. Adiabatic effectiveness contours in this paper are split into three parts, where hole (a) is a singular hole over the smooth surface (from Schroeder and Thole [4]), holes (b-d) are the center three measured holes over the 0 deg 5HS surface, and holes (e-g) are the three measured holes over the 90 deg 5HS surface. Three holes are included in the contours for the CMC surfaces because the hole footprint and near-hole surface topography vary between holes. Note that the contours include shading to relate the underlying CMC surface pattern to the measured adiabatic effectiveness.

The coolant pattern of the smooth surface in Fig. 5(a) [4] and 0 deg 5HS surface in Figs. 5(b)-5(d) are similar in overall shape, but have a few important differences. The 0 deg 5HS surface has lower effectiveness values relative to the smooth surface across most of the domain; this is particularly noticeable along the centerline in both the near-hole region and further downstream past $x/D = 20$. Another feature of the 0 deg 5HS surface is the small but visible impact of the cross-tows causing local increases and decreases in cooling effectiveness across the CMC surface. An example of the

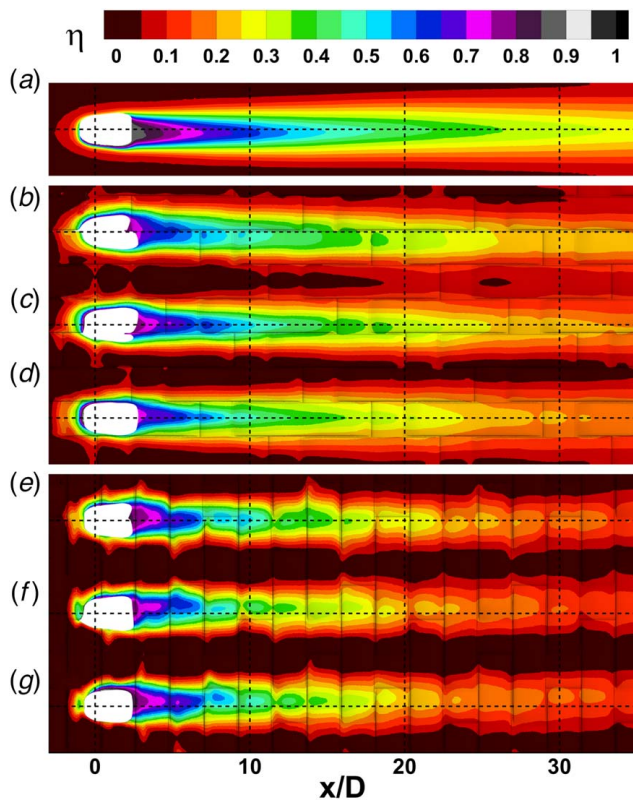


Fig. 5 Adiabatic effectiveness contours at 0.5% freestream turbulence and $M=1.5$ over the (a) smooth surface [4], (b) 0 deg 5HS surface hole b, (c) 0 deg 5HS surface hole c, (d) 0 deg 5HS surface hole d, (e) 90 deg 5HS surface hole e, (f) 90 deg 5HS surface hole f, and (g) 90 deg 5HS surface hole g

behavior is present in Fig. 5(c) at $15 < x/D < 20$ where there is a small decrease in effectiveness as a long “A” tow transitions to a small “B” cross-tow. The effectiveness increases slightly at the top of the small cross-tow but then decreases again as the small cross-tow transitions back to a long tow. These local variations are caused by the jet interacting with the separation and reattachment flow features around the tow transitions measured by Wilkins et al. [3].

On the 90 deg surface, the local impact of the large cross-tows is much greater than it is for the 0 deg case as a result of the larger number of tow interfaces oriented perpendicular to the freestream. The blockage introduced by the front-facing tows causes coolant to flow laterally away from the centerline, resulting in a local increase in lateral spreading over the 90 deg surface. Additionally, the 90 deg orientation has local decreases in adiabatic effectiveness between perpendicular tows along the centerline due to coolant passing over the small gaps between tows. These gaps transition to islands of locally higher effectiveness located on the tops of tows where the coolant jet re-contacts the surface. Overall, the lateral spreading on the 90 deg surface is reduced relative to both the 0 deg and smooth surfaces which is indicative of increased jet detachment.

For the higher blowing ratio of 3.0, shown in Fig. 6, the lateral spreading for all of the surfaces is reduced compared to the $M=1.5$ cases. This spreading results at high blowing ratios because the coolant jet detaches from the surface, shifting the jet away from the wall. Along the centerline of the smooth surface in Fig. 6(a), effectiveness values are comparable to the centerline values in the lower blowing ratio case in Fig. 5(a), but with reduced lateral spreading. However, this trend does not hold true for most of the CMC test cases. On the 0 deg surface, the centerline effectiveness of the holes in Figs. 6(b) and 6(c) increase at $M=3.0$ relative to $M=1.5$ (Figs. 5(b) and 5(c)), while the centerline

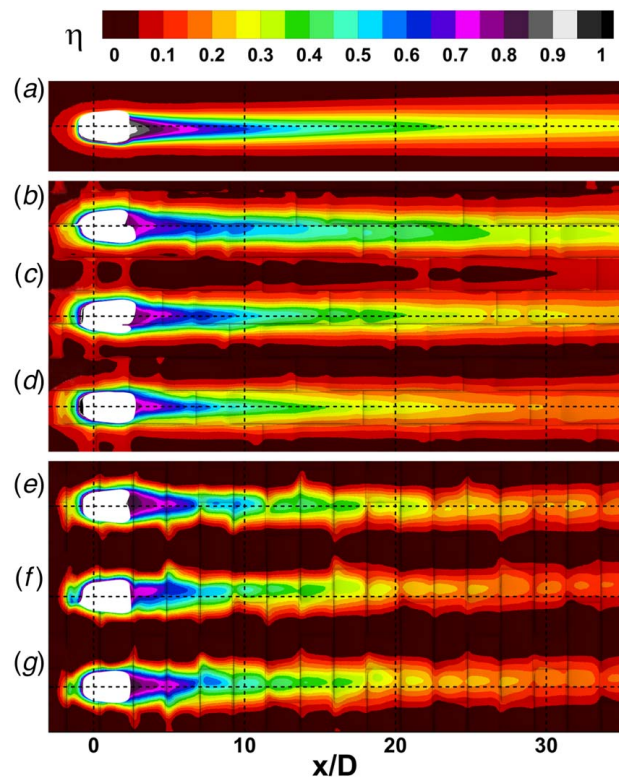


Fig. 6 Adiabatic effectiveness contours at 0.5% freestream turbulence and $M=3.0$ over the (a) smooth surface [4], (b) 0 deg 5HS surface hole b, (c) 0 deg 5HS surface hole c, (d) 0 deg 5HS surface hole d, (e) 90 deg 5HS surface hole e, (f) 90 deg 5HS surface hole f, and (g) 90 deg 5HS surface hole g

effectiveness in Fig. 6(d) is similar to the $M=1.5$ case. Another feature of the 0 deg surface is the dissimilarity between the coolant patterns of the individual holes shown in Figs. 6(b)–6(d) at $M=3.0$. This dissimilarity suggests that at high blowing ratios the small changes in surface outlet shape and the surface features directly downstream of the hole exit are more influential than at low blowing ratios.

Some variation between individual coolant holes is also present over the 90 deg surface shown in Figs. 6(e)–6(g), but relative to the 0 deg surface, the variation is much less. This is likely because the spanwise oriented tows of the 90 deg surface are already a significant blockage to the film jet, which makes it somewhat insensitive to blowing ratio. Notably, the local disturbances of the adiabatic effectiveness are similar between the $M=1.5$ and $M=3.0$ cases for the 90 deg surface. An example of this behavior is in Fig. 6(g) at $x/D=8$ where the coolest part of the surface is shifted away from the centerline but has nearly the same effectiveness for $M=1.5$ as for $M=3.0$.

Laterally averaged adiabatic effectiveness for the smooth and CMC surfaces is shown in Fig. 7. Note that the lateral average is taken over the three center holes for both smooth and CMC surfaces. At $M=1.5$ the smooth surface [4] outperforms all of the other cases. The 0 deg CMC surface at $M=1.5$ is the closest to the smooth surface, while the 90 deg CMC surface has the worst overall laterally averaged effectiveness at that blowing ratio. Additionally, the high variation of the lateral average with x/D portrays the impact of the forward-facing tows of the 90 deg surface in locally disturbing lateral spreading of the coolant.

At the high blowing ratio of $M=3$, there is a large decrease in laterally averaged adiabatic effectiveness relative to $M=1.5$ for the smooth surface [4] due to the narrowing of the coolant jet. Comparatively, laterally averaged cooling effectiveness over the two CMC surfaces is only minimally impacted at $M=3$. The 0 deg surface has an effectiveness that is slightly lower for $M=3$

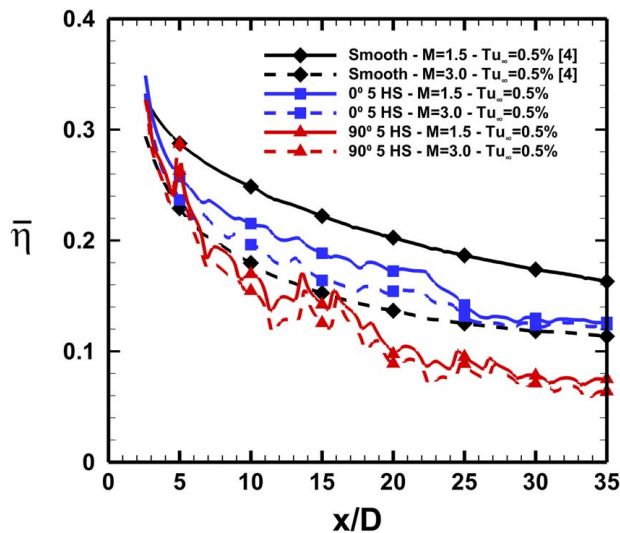


Fig. 7 Laterally averaged adiabatic effectiveness of the smooth [4] and CMC surfaces at 0.5% freestream turbulence

compared to $M = 1.5$, but at downstream locations greater than $x/D = 25$ it is nearly identical for both blowing ratios. The 90 deg surface exhibits an even smaller difference between $M = 1.5$ and $M = 3.0$. This suggests that the presence of the CMC surface roughness does disturb film cooling relative to a smooth surface but the roughness reduces sensitivity to blowing ratio.

High Freestream Turbulence Adiabatic Effectiveness. High freestream turbulence is a common occurrence within gas turbines [33] and is known to have an important impact on smooth surface film cooling. To investigate the impact of high turbulence on CMC film cooling, the same surface geometries and test conditions are investigated at a freestream turbulence level of 13%. In Fig. 8, the adiabatic effectiveness contours for $M = 1.5$ at the freestream turbulence intensity of 13% are shown. The smooth surface in Fig. 8(a) [5] has more lateral spreading at $Tu_{\infty} = 13\%$ than at $Tu_{\infty} = 0.5\%$ (Fig. 5(a)), in addition to a drop in centerline effectiveness. As described by Schroeder and Thole [5], this is due to the turbulence causing increased dissipation of the low-blowing ratio jet.

The CMC surface changes the response of the film to freestream turbulence at low blowing ratio conditions relative to the smooth surface. The 0 deg surface at $Tu_{\infty} = 13\%$ and $M = 1.5$ in Figs. 8(b)–8(d) has slightly less lateral spreading (particularly around $2 < x/D < 10$) with a higher downstream decay compared to the $Tu_{\infty} = 0.5\%$ cases in Fig. 5, with virtually no coolant present after $x/D = 23$. At 13% turbulence over the 0 deg surface, the impact of individual rows on coolant uniformity is not readily visible like it is for the 0.5% turbulence case.

The 90 deg surface also exhibits a marked reduction in downstream cooling at high turbulence, with virtually no coolant present beyond $x/D = 23$. However, the overall lateral spreading and localized impact of long tow features in the 13% turbulence case in Figs. 8(d)–8(f) is similar to the 0.5% Tu case (Figs. 5(d)–5(f)). Thus, the flow disturbance caused by the forward-facing rows is still important even at high turbulence levels.

At a high blowing ratio for the 13% freestream turbulence intensity, the smooth surface shown in Fig. 9(a) [5] has lower centerline effectiveness values but better lateral spreading than the low turbulence case in Fig. 6(a) [4]. Note also that this high-blowing ratio case has higher centerline effectiveness but slightly reduced spreading relative to the low-blowing ratio high turbulence case in Fig. 8(a). For smooth surfaces, high freestream turbulence improves jet attachment at a high blowing ratio relative to low turbulence intensities, but for a fixed level of high freestream turbulence, a

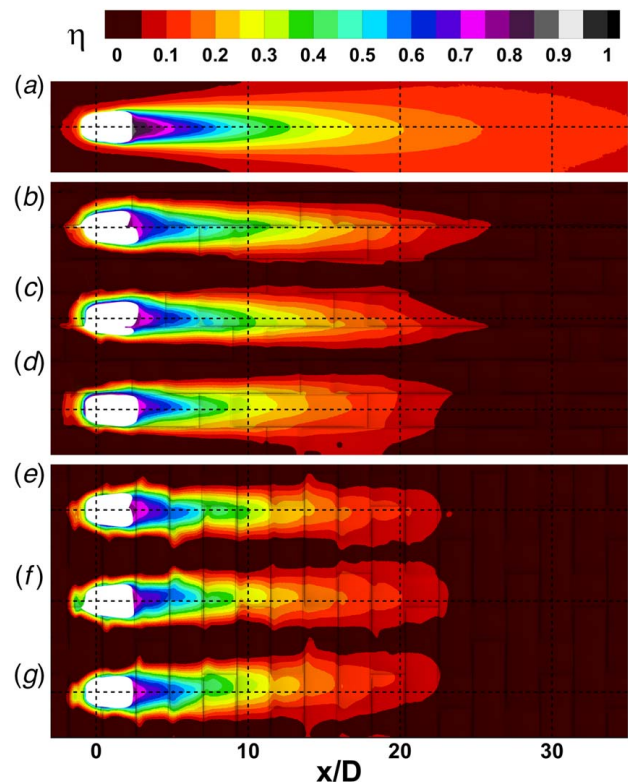


Fig. 8 Adiabatic effectiveness contours at 13% freestream turbulence and $M = 1.5$ over the (a) smooth surface [5], (b) 0 deg 5HS surface hole b, (c) 0 deg 5HS surface hole c, (d) 0 deg 5HS surface hole d, (e) 90 deg 5HS surface hole e, (f) 90 deg 5HS surface hole f, and (g) 90 deg 5HS surface hole g

high blowing ratio still exhibits some jet detachment behavior relative to a low blowing ratio.

Again, these trends do not uniformly carry over to the CMC surfaces. For the 0 deg surface in Figs. 9(b)–9(d) there is a drop in both centerline effectiveness and overall lateral spreading compared to the low turbulence case in Figs. 6(b)–6(d). Note that the local diversion of coolant around the tow transitions is less apparent in the high turbulence case. One positive change for the 0 deg surface is the increase in uniformity between the holes at the higher turbulence level. When comparing low to high blowing ratio at a fixed high turbulence intensity (Figs. 8(b)–8(d) versus 9(b)–9(d)), the high blowing ratio case has higher centerline effectiveness and slightly reduced spreading as expected for increasing jet detachment behavior.

The 90 deg surface shown in Figs. 9(e)–9(g) is similar in the near-hole region to the low turbulence case in Figs. 6(e)–6(g), but with reduced centerline effectiveness further downstream and a marked increase in lateral spreading past $x/D = 15$ at high freestream turbulence. Also, a slight improvement in effectiveness is observed as the blowing ratio increases from low (Figs. 8(b)–8(d)) to high (Figs. 9(b)–9(d)) values at a similar high turbulence level, likely due to the combination of the forward-facing rows and high turbulence which leads to repeated jet detachment and dissipation.

The lateral average of the high freestream turbulence film cooling cases is shown in Fig. 10, where the CMC surfaces have reduced performance compared to the smooth surface [5] across the range of blowing ratios investigated. Reductions in film effectiveness due to the CMC surface vary depending on the blowing ratio, with the low blowing ratio cases, $M = 1.5$, resulting in the largest decreases in cooling effectiveness relative to the smooth surface. Upstream of $x/D = 20$, both CMC orientations across the range of blowing ratios tested have similar lateral averages. This is unlike the result observed in Fig. 7 for low turbulence, suggesting that

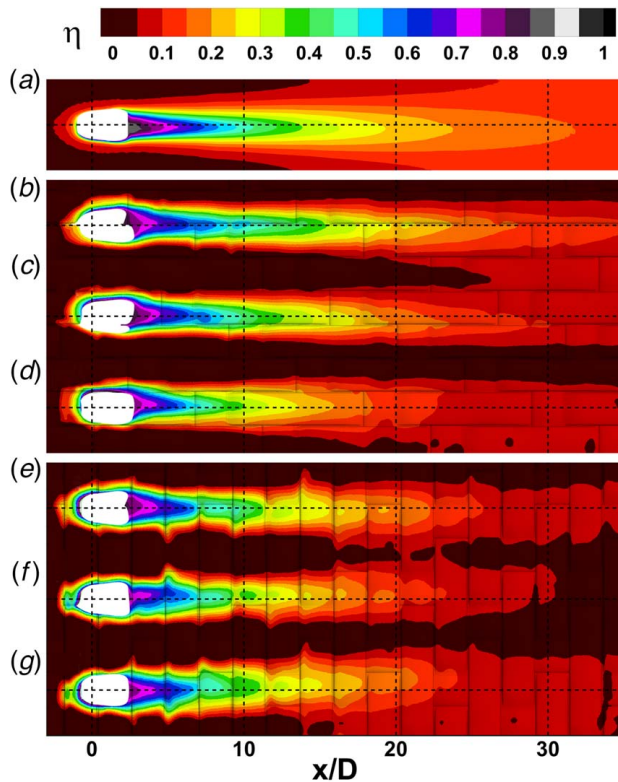


Fig. 9 Adiabatic effectiveness contours at 13% freestream turbulence and $M=3.0$ over the (a) smooth surface [5], (b) 0 deg 5HS surface hole b, (c) 0 deg 5HS surface hole c, (d) 0 deg 5HS surface hole d, (e) 90 deg 5HS surface hole e, (f) 90 deg 5HS surface hole f, and (g) 90 deg 5HS surface hole g

the 0 deg surface is more detrimentally impacted by freestream turbulence than the 90 deg surface. This result is not so surprising given that the 0 deg surface has behaviors more similar to a smooth surface than to its 90 deg counterpart. Past $x/D=20$, the $M=3.0$ cases have higher laterally averaged effectiveness relative to the $M=1.5$ cases, suggesting that the main impact of increasing the blowing ratio over the CMC surface at $Tu_\infty=13\%$ is to increase the distance that coolant persists downstream.

Area-averaged adiabatic effectiveness in the near-hole region between $3 < x/D < 15$ is shown in Fig. 11 for the experimental

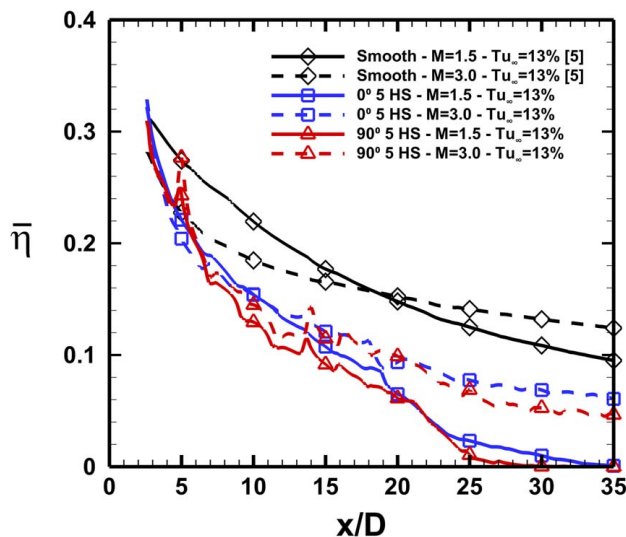


Fig. 10 Laterally averaged adiabatic effectiveness of the smooth [5] and CMC surfaces at 13% freestream turbulence

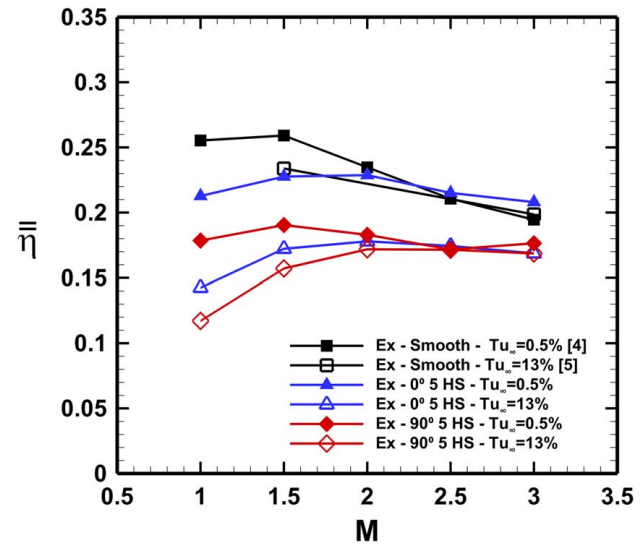


Fig. 11 Area-averaged adiabatic effectiveness from $3 < x/D < 15$ for the smooth surface [4,5] and CMC surfaces

data presented in this paper and from Schroeder and Thole [4,5]. In general, all cases indicate a maximum level of effectiveness at $M=1.5$ and decreasing effectiveness at high M , which matches the conclusions of Schroeder and Thole [4] for the smooth surface. At the optimum blowing ratio of 1.5, the smooth surface at low Tu_∞ has the highest effectiveness and the 90 deg 5HS weave at $Tu_\infty=13\%$ is nearly 38% lower, due to the aforementioned significant interaction between the forward-facing rows, freestream turbulence, and the coolant jet. However, as the blowing ratio increases the area-averaged effectiveness tends to become similar for all cases, as jet detachment begins to dominate the cooling behavior.

The 0 deg 5HS surface performs the closest out of the two weave patterns to the smooth surface, even performing slightly better than the smooth surface at $M=3.0$ and $Tu_\infty=0.5\%$. Compared to the smooth surface, it has somewhat less sensitivity to blowing ratio, with similar area-average effectiveness values across the tested range. The 0 deg 5HS surface also exhibits a nearly constant drop in effectiveness between low and high Tu_∞ conditions over the range of blowing ratios. This behavior is dissimilar to the smooth surface, which has a drop in effectiveness at low M but nearly the same effectiveness at high M due to the competing effects of decreased centerline effectiveness but improved lateral spreading (see Figs. 6(a)–9(a)).

For the 90 deg surface results in Fig. 11, its performance is quite low at low blowing ratios and is further reduced with high freestream turbulence. However, unlike the 0 deg surface, the reduction in effectiveness due to turbulence tapers off above $M=2$. The similar performance between the 90 deg surface at the two measured turbulence levels indicates a low sensitivity to freestream turbulence level or tow orientation at moderate to high blowing ratios. At low turbulence, the 90 deg surface is always lower effectiveness than the 0 deg surface, while at high turbulence, both surface orientations result in similar average effectiveness over the blowing ratio range tested.

Comparing previous low turbulence ($Tu_\infty=0.5\%$) computational fluid dynamics (CFD) results by Wilkins et al. [18] over the CMC surfaces with experimental data from this study results in similar trends of locally high and low adiabatic effectiveness are present across the same surface features. However, across the surface, the CFD poorly predicts overall trends, including lateral and area averages, where sharper gradients of effectiveness between surface features are present when compared to the experimental results.

Flowfield Measurements. PIV measurements are taken for a select number of freestream turbulence and blowing ratio cases over each CMC surface to provide a detailed picture of the interaction between the coolant jets and the mainstream. Measurements are taken along the centerline of the center hole, extending upstream to $x/D = -4$ and downstream to $x/D = 15$ and are compared to the smooth surface measurements taken by Schroeder and Thole [5].

Figure 12 shows streamwise time-average velocity contours for both the smooth and CMC surfaces at two blowing ratios, at a low turbulence level of 0.5%. At the low blowing ratio of $M = 1.5$ in Fig. 12(a), the coolant jet over the smooth surface is attached to the wall, with low velocities in the near-wall region downstream of the hole. The jet core is more clearly distinguished in the higher blowing ratio smooth surface results in Fig. 12(b), where the high-velocity jet (values of $U/U_\infty > 1$) disrupts the boundary layer and detaches from the downstream surface. This results in reduced

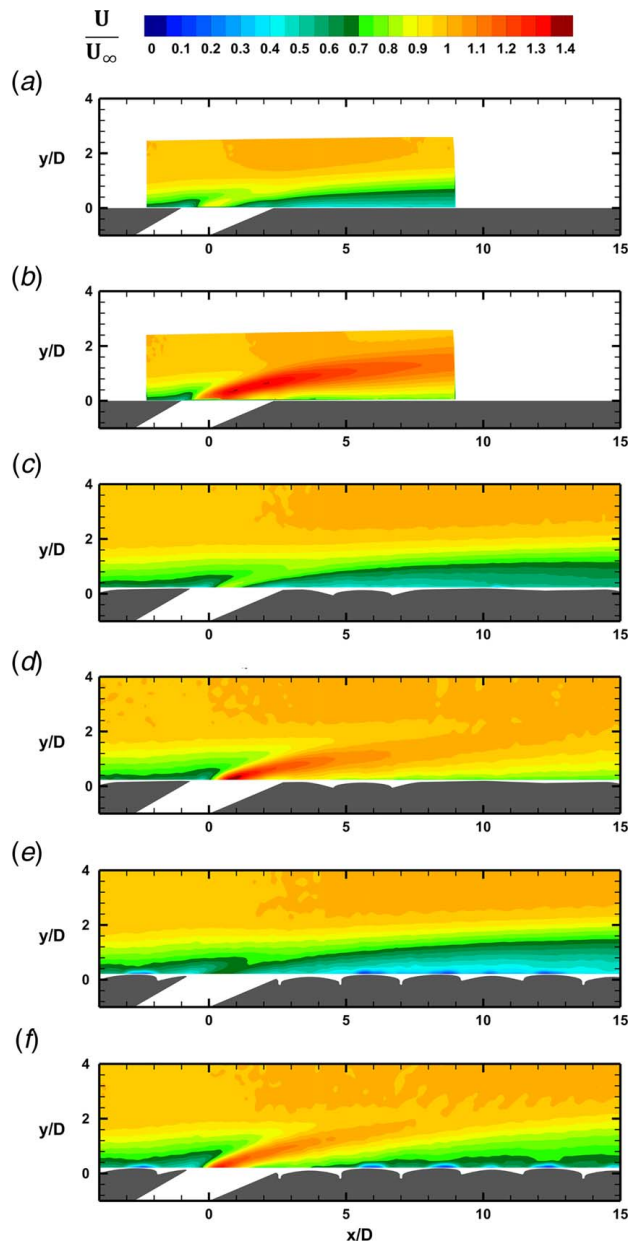


Fig. 12 Velocity contours from centerline PIV measurements at $Tu_\infty = 0.5\%$ for (a) smooth surface— $M = 1.5$ [5], (b) smooth surface— $M = 3.0$ [5], (c) 0 deg 5HS surface— $M = 1.5$, (d) 0 deg 5HS surface— $M = 3.0$, (e) 90 deg 5HS surface— $M = 1.5$, and (f) 90 deg 5HS surface— $M = 3.0$

Table 1 Incoming boundary layer characteristics

Surface	Tu_∞	δ_{99}/D	θ/D	H	Re_θ
Smooth [5]	0.5%	1.07	0.14	1.45	670
Smooth [5]	13%	1.21	0.12	1.38	580
0 deg 5HS	0.5%	1.95	0.24	1.26	1000
0 deg 5HS	13%	2.68	0.22	1.12	930
90 deg 5HS	0.5%	2.79	0.29	1.42	1200
90 deg 5HS	13%	3.2	0.25	1.15	1100

coolant spreading relative to the $M = 1.5$ case as shown in Figs. 5(a)–6(a) [5].

When comparing the CMC surfaces in Fig. 12 to the smooth surface, one expected observation is the thicker incoming boundary layer upstream of the hole for the CMC surfaces. The incoming boundary layer characteristics are also shown in Table 1. The roughness of the CMC surfaces leads to more significant boundary layer development.

Other than a difference in incoming boundary layer thickness, the 0 deg 5HS surface at $M = 1.5$ shown in Fig. 12(c) results in similar streamwise velocity in the region downstream of the coolant injection. This follows from the earlier observations that the 0 deg CMC surface is closest in adiabatic effectiveness to the smooth surface. The PIV system is unable to measure into the crevices of the tow transitions around $x/D = 4$ and 6, but previous measurements by Wilkins et al. [3] indicated small separations and reattachments around the transitions.

For the 0 deg CMC surface with a high blowing ratio in Fig. 12(d), the jet core is visible as a high-velocity region; however, it does not persist as long as the smooth surface high blowing ratio case in Fig. 12(b). As will be shown later, the shear layer between the jet and the incoming thick boundary layer over the CMC is strengthened, resulting in increased dissipation of the jet core velocity and reduced cooling effectiveness (Fig. 6) as the jet is mixed out with the freestream.

Over the 90 deg 5HS surface in Fig. 12 there is a significant region of low velocity both around the hole exit and downstream of the hole for the low blowing ratio case (Fig. 12(e)), which is much lower than for both the 0 deg and smooth surfaces. This is due to the recirculations around the tow transitions for the 90 deg CMC surface that dominate the near-wall region. Likewise, the $M = 3.0$ case in Fig. 12(f) shows similar influences of the weave pattern on the velocity near the wall. This low-velocity region acts to keep the jet away from the wall, increasing the penetration angle between the jet and the wall relative to the 0 deg and smooth surfaces. This conclusion is reinforced by the limited lateral spreading present in Figs. 5(e)–5(g) and Figs. 6(e)–6(g), which is characteristic of jet detachment over a surface.

Streamwise time-averaged velocity contours at $Tu_\infty = 13\%$ in Fig. 13 are broadly similar to the low turbulence cases, with a few notable differences. Over the smooth surface at $M = 1.5$ and $M = 3.0$ in Figs. 13(a) and 13(b) [5], both the jet and near-wall velocities downstream of the cooling holes are higher for the $Tu_\infty = 13\%$ cases relative to the low Tu_∞ cases in Fig. 12, as the high turbulence tends to bring high momentum fluid close to the wall. The CMC surfaces in Figs. 13(c)–13(f) generally exhibit this same behavior, where high turbulence results in higher near-wall velocity downstream of the jet. In the case of low blowing ratios, this phenomenon tends to dissipate the coolant jet since the high momentum is outside the jet core, but for high blowing ratios, the coolant can be brought back down to the wall by turbulent motions.

Figure 13 also may explain the reduced sensitivity to blowing ratio observed in the effectiveness results for the CMC surfaces. For the smooth surface, there is a significant difference in near-wall velocity downstream of the hole between the low (Fig. 13(a)) and high (Fig. 13(b)) blowing ratio cases. However, there is less difference in near-wall velocity for the two CMC surfaces between low

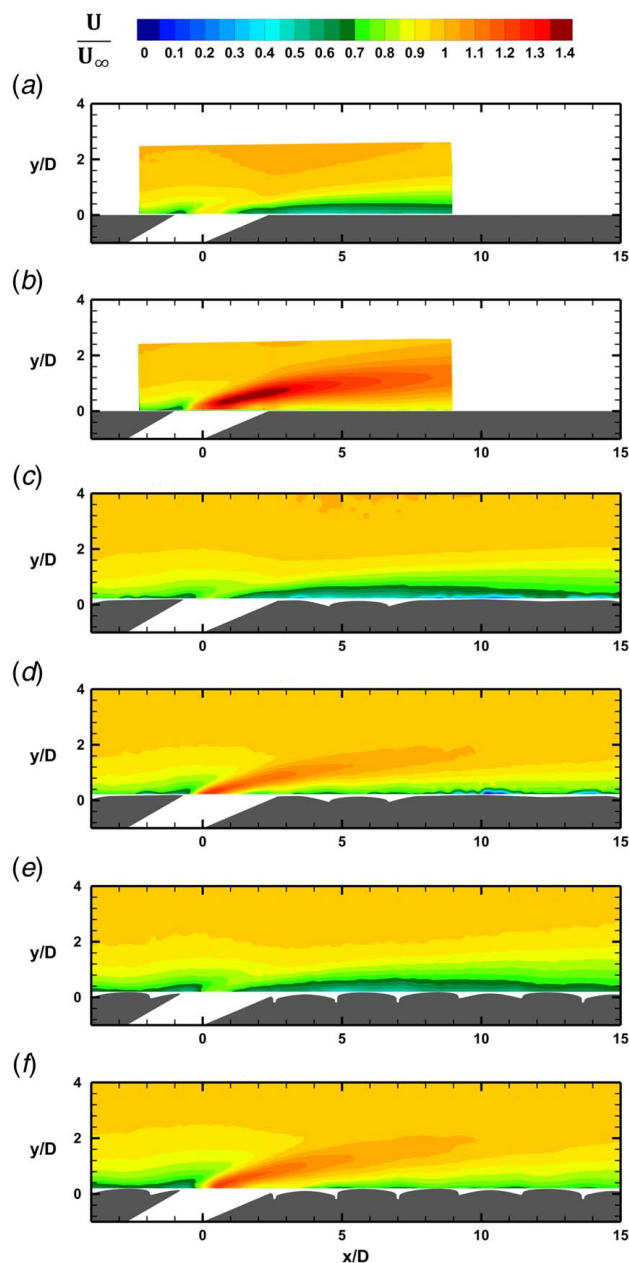


Fig. 13 Velocity contours from centerline PIV measurements at $Tu_\infty = 13\%$ for (a) smooth surface— $M = 1.5$ [5], (b) smooth surface— $M = 3.0$ [5], (c) 0 deg 5HS surface— $M = 1.5$, (d) 0 deg 5HS surface— $M = 3.0$, (e) 90 deg 5HS surface— $M = 1.5$, and (f) 90 deg 5HS surface— $M = 3.0$

and high blowing ratios, or even between the two types of CMC surfaces at a given blowing ratio. This aligns with the findings in Fig. 11 regarding effectiveness values remaining rather unchanged with the blowing ratio for CMC surfaces.

Turbulence intensity along the center plane is shown in Fig. 14 for select cases at $M = 3.0$. The smooth surface at a freestream turbulence level of 0.5% and the blowing ratio $M = 3.0$ in Fig. 14(a) [5] shows an increase in turbulence intensity at the hole exit, which Schroeder and Thole [5] suggested is a combination of flow separation within the hole and a shear layer developing between the jet and incoming flow. The 0 deg surface in Fig. 4(b) has a broadly similar turbulence profile to the smooth surface, with an elevated region of turbulence at the hole exit that dissipates as the jet moves downstream. However, over the 0 deg surface, the turbulence intensity rapidly decreases with downstream distance than over the smooth surface and largely stays within the boundary layer. The high level of turbulence already presents near

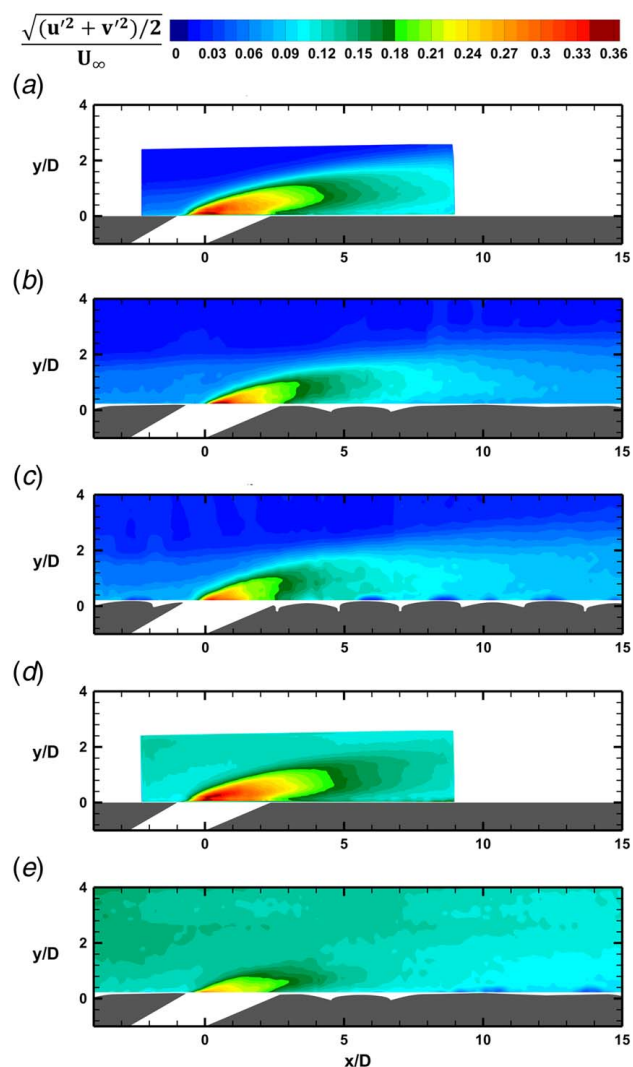


Fig. 14 Turbulence intensity contours for (a) smooth surface— $Tu_\infty = 0.5\%$ — $M = 3.0$ [5], (b) 0 deg 5HS surface— $Tu_\infty = 0.5\%$ — $M = 3.0$, (c) 90 deg 5HS surface— $Tu_\infty = 0.5\%$ — $M = 3.0$, (d) smooth surface— $Tu_\infty = 13\%$ — $M = 3.0$ [5], (e) 0 deg 5HS surface— $Tu_\infty = 13\%$ — $M = 3.0$

the wall for the 0 deg CMC surface may increase the dissipation of the jet shear layer leading to fewer large-scale turbulent motions. This could also be a mechanism responsible for the 0 deg surface outperforming the smooth surface at $M = 3$ in Fig. 7.

Over the 90 deg surface at $M = 3.0$, turbulence intensity right around the hole exit in Fig. 14(c) is slightly reduced compared to the 0 deg surface in Fig. 14(b). However, downstream of the hole, the turbulence generated by the jet does not dissipate as quickly for the 90 deg case compared to the 0 deg case.

The smooth surface in Fig. 14(d) and the 0 deg surface in Fig. 14(e) show the impact of elevated turbulence on a coolant jet at $M = 3.0$. Note the overall high levels of turbulence intensity in the freestream in Figs. 14(d) and 14(e). Over the smooth surface in Fig. 14(d) the turbulence from the jet is similar to the low turbulence case in Fig. 14(a). Comparing the 0 deg 5HS surface at the $Tu_\infty = 13\%$ case (Fig. 14(e)) to the $Tu_\infty = 0.5\%$ case (Fig. 14(b)), the turbulence around the hole exit is reduced for the high freestream turbulence case. Downstream of the hole, turbulence intensity from the jet is similar to or slightly lower than the freestream turbulence intensity, suggesting that the freestream turbulence is a dominant phenomenon causing additional mixing between the mainstream and coolant. This behavior is broadly similar for the 90 deg surface, which is not shown for brevity.

Figure 15 shows Reynolds shear stresses for select cases at a high blowing ratio. The smooth surface at $M = 3.0$ and $Tu_\infty = 0.5\%$ [5] is shown in Fig. 15(a), where a region of positive Reynolds stress on the upstream side of the hole exit is generated by the high-velocity coolant interacting with the freestream creating a shear layer. The negative region on the downstream side of the hole exit, due to the underside of the jet shear layer, moves away from the wall as it continues downstream.

Over the 0 deg CMC surface in Fig. 15(b) at $M = 3.0$, $Tu_\infty = 0.5\%$ the Reynolds stress is broadly similar to the smooth surface (Fig. 15(a)) with a region of positive Reynolds stress at the leading edge of the jet and negative stress on the trailing edge. However, the positive Reynolds stress for the 0 deg CMC has a greater magnitude near the hole and dissipates faster than the smooth surface downstream. The region of negative Reynolds stress over the 0 deg surface has a reduced magnitude and is closer to the wall than the smooth surface case, where for this surface there could be some increased contribution of wall-originating turbulent motions. For the 90 deg CMC surface, the positive region of Reynolds stress in Fig. 15(c) is smaller than over the 0 deg surface (Fig. 15(b)) while the negative region is both more persistent and has a wider dispersion. It is highly likely that wall-originating turbulent motions are dominant for this surface, as evidenced by the

disruption of coolant (Figs. 6(e)–6(g)), as well as the near-wall turbulence measurements of Wilkins et al. [3].

At $Tu_\infty = 13\%$, $M = 3.0$ the smooth surface [5] in Fig. 15(d) has regions of Reynolds stress that are both greater in magnitude and with wider extent than the $Tu_\infty = 0.5\%$ case in Fig. 15(a). These larger regions of Reynolds stress imply increased mixing between the freestream and coolant jet, resulting in the reduced cooling effectiveness at low blowing ratios and increased effectiveness at downstream locations for high blowing ratios as noted by Schroeder and Thole [5]. In contrast, the positive Reynolds stress for the 90 deg CMC surface at high turbulence and high blowing ratio (Fig. 15(e)) is reduced relative to the smooth surface, while the region of negative Reynolds stress is larger and persists downstream a greater distance. Note also the high levels of negative Reynolds stress upstream of the hole for this particular case; we conjecture that the freestream turbulence interacts in a positive-feedback manner with the wall-originating turbulence from the 90 deg CMC surface.

Conclusions

In this study, we present experimental measurements of film cooling from 7–7 shaped holes embedded in a simulated CMC weave surface (specifically a 5HS pattern). The measurements are taken over a range of blowing ratios and freestream turbulence levels for two orientations of the weave surface. Time-resolved particle image velocimetry measurements are also taken for select cases to understand the flowfield resulting from film cooling over a CMC.

In most cases, film cooling over a CMC surface results in a loss of cooling effectiveness compared to a smooth surface. For both CMC surfaces increased mixing between the coolant jet and the mainstream is one of the dominating mechanisms that cause the reduction in cooling effectiveness. However, at high blowing ratio conditions where jet detachment can occur, the combination of increased turbulent mixing and a thicker approach boundary layer help recirculate detached coolant back to the wall; similar to the behavior that Schroeder and Thole [5] observed for smooth surfaces at high freestream turbulence.

The loss of cooling performance is dependent on the orientation of the weave, where the 0 deg surface outperforms the 90 deg surface across the range of blowing ratios tested. Some of the key factors responsible for poor cooling performance over the 90 deg surface include a reduction of jet velocity, increased jet detachment from the wall, and increased mixing between the jet and the mainstream relative to the 0 deg and smooth surfaces. One positive impact of the aforementioned behaviors is the insensitivity of the 90 deg surface to blowing ratio.

Introducing high levels of freestream turbulence results in a loss of adiabatic effectiveness for both CMC surfaces relative to low turbulence intensities, as the roughness and turbulence have a synergistic effect at blowing ratios below $M = 2.0$. This leads to strong mixing that overwhelms the jet structure, which in turn contributes to more coolant mixing away from the wall. The addition of elevated turbulence causes the higher blowing ratio cases to have less film effectiveness decay past $x/D = 25$ for all of the surfaces but is particularly prevalent for the CMC cases.

Overall, our findings indicate that it is important to account for the surface geometry of CMCs in designing film cooling. Future work should expand upon the types of surface geometries investigated beyond the single weave pattern used in this paper while also looking to incorporate anisotropy of CMCs with their unique surface topographies.

Acknowledgment

The authors would like to thank Pratt & Whitney for their generous support throughout the duration of this project.

Conflict of Interest

There are no conflicts of interest.

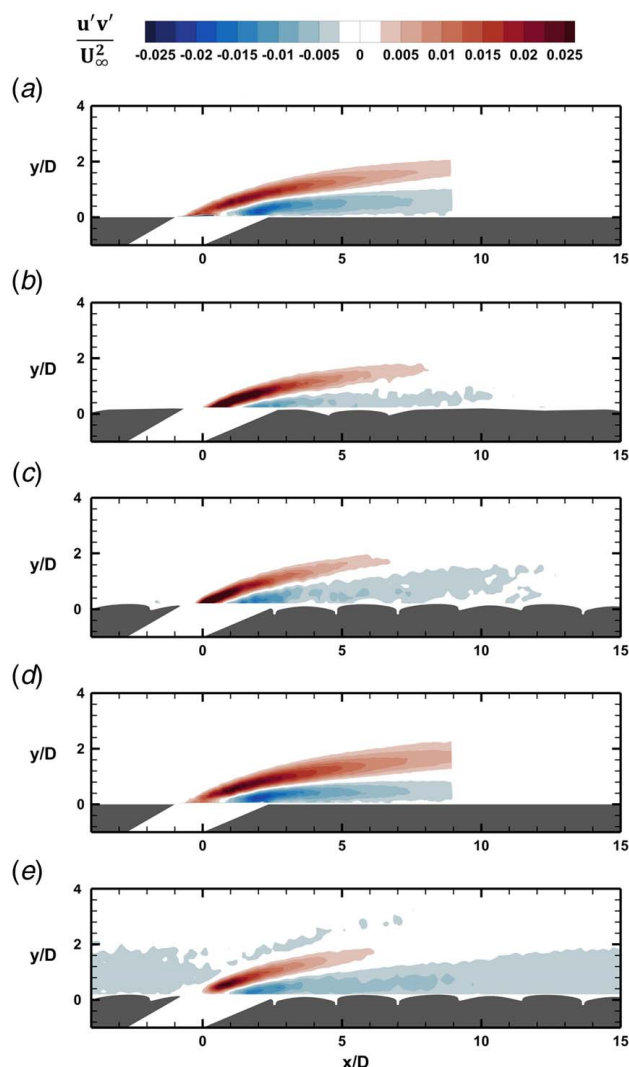


Fig. 15 Reynolds shear stress contours for (a) smooth surface— $Tu_\infty = 0.5\%$ — $M = 3.0$ [5], (b) 0 deg 5HS surface— $Tu_\infty = 0.5\%$ — $M = 3.0$, (c) 90 deg 5HS surface— $Tu_\infty = 0.5\%$ — $M = 3.0$, (d) smooth surface— $Tu_\infty = 13\%$ — $M = 3.0$ [5], (e) 90 deg 5HS surface— $Tu_\infty = 13\%$ — $M = 3.0$

Data Availability Statement

The datasets generated and supporting the findings of this article are obtainable from the corresponding author upon reasonable request.

Nomenclature

b = turbulence grid bar diameter
 k = thermal conductivity
 x = streamwise direction
 y = wall normal direction
 z = spanwise direction
 A = hole cross-sectional area
 D = diameter of film cooling holes
 H = boundary layer shape factor, $H = \delta^*/\theta$
 L = film cooling hole length
 M = blowing ratio, $\rho_c U_c / \rho_\infty U_\infty$
 P = pitch between film cooling holes
 T = temperature
 U = mean streamwise velocity
 Re_x = Reynolds number, $Re_x = U_\infty x / \nu$
 Re_θ = momentum thickness Reynolds number,
 $Re_\theta = U_\infty \theta / \nu$
 S_a = arithmetic mean roughness
 S_q = root mean square roughness
 S_z = maximum roughness height
 DR = density ratio, ρ_c / ρ_∞
 Tu = turbulence intensity, $Tu = \sqrt{(u_\infty^2 + v_\infty^2)} / 2 / U_\infty$

Greek Symbols

α = hole injection angle
 β = expansion angle for diffused outlet
 δ_{99} = boundary layer thickness
 δ^* = displacement thickness
 η = local adiabatic effectiveness $(T_\infty - T_{aw}) / (T_\infty - T_c)$
 θ = momentum thickness
 λ = tow width
 ν = kinematic viscosity
 ρ = density

Subscripts

c = coolant, at hole inlet
 m = metering section
 air = property of air
 aw = adiabatic wall
 CMC = property of CMC surface test plate
 $diff$ = diffuser section
 $exit$ = exit plane of the film cooling hole
 fwd = forward expansion of shaped hole
 $inlet$ = inlet plane of the film cooling hole
 lat = lateral expansion of shaped hole (half-angle)
 $measured$ = measured value
 0 = property of a flat surface
 0 = conduction altered surface temperature
 ∞ = freestream
 $'$ = fluctuating/rms value
 $-$ = laterally averaged
 $=$ = area averaged

References

- [1] Levine, S. R., 1992, "Ceramics and Ceramic Matrix Composites—Aerospace Potential and Status," Proceedings of the Structures, Structural Dynamics and Materials Conference, Dallas, TX, AIAA Paper No. AIAA-92-2445-CP, pp. 1942–1947.
- [2] Krenkel, W., 2008, *Ceramic Matrix Composites Fiber Reinforced Ceramics and Their Applications*, Wiley-VCH Verlag GmbH & Co. KGaA, Weinheim, Germany.
- [3] Wilkins, P. H., Lynch, S. P., Thole, K. A., Quach, S., and Vincent, T., 2020, "Experimental Heat Transfer and Boundary Layer Measurements on a Ceramic Matrix Composite Surface," *ASME J. Turbomach.*, **143**(6), p. 061010.
- [4] Schroeder, R. P., and Thole, K. A., 2014, "Adiabatic Effectiveness Measurements for a Baseline Shaped Film Cooling Hole," Proceedings of the ASME Turbo Expo, Dusseldorf, Germany, June 16–20, ASME Paper No. GT2014-25992.
- [5] Schroeder, R. P., and Thole, K. A., 2016, "Effect of High Freestream Turbulence on Flowfields of Shaped Film Cooling Holes," *ASME J. Turbomach.*, **138**(9), p. 091001.
- [6] Bryant, C. E., and Rutledge, J. L., 2021, "Conjugate Heat Transfer Simulations to Evaluate the Effect of Anisotropic Thermal Conductivity on Overall Cooling Effectiveness," *ASME J. Therm. Sci. Eng. Appl.*, **13**(6), p. 061013.
- [7] Tu, Z., Mao, J., and Han, X., 2017, "Numerical Study of Film Cooling Over a Flat Plate With Anisotropic Thermal Conductivity," *Appl. Therm. Eng.*, **111**, pp. 968–980.
- [8] Tu, Z., Mao, J., Han, X., and He, Z., 2019, "Experimental Study of Film Cooling Over a Fiber-Reinforced Composite Plate With Anisotropic Thermal Conductivity," *Appl. Therm. Eng.*, **148**, pp. 447–456.
- [9] Prokein, D., von Wolfersdorf, J., Dittert, C., and Böhrk, H., 2018, "Transpiration Cooling Experiments on a CMC Wall Segment in a Supersonic Hot Gas Channel," International Energy Conversion Engineering Conference, Cincinnati, OH, July 9–11, AIAA Paper No. AIAA 2018-4696.
- [10] Zhong, F., and Brown, G. L., 2009, "Experimental Study of Multi-Hole Cooling for Integrally-Woven, Ceramic Matrix Composite Walls for Gas Turbine Applications," *Int. J. Heat Mass Transf.*, **52**(3–4), pp. 971–985.
- [11] Goldstein, R. J., Eckert, E. R. G., Chiang, H. D., and Elovic, E., 1985, "Effect of Surface Roughness on Film Cooling Performance," *ASME J. Eng. Gas Turbines Power*, **107**(1), pp. 111–116.
- [12] Barlow, D. N., and Kim, Y. W., 1995, "Effect of Surface Roughness on Local Heat Transfer and Film Cooling Effectiveness," Proceedings of the ASME Turbo Expo, Houston, TX, June 5–8, 1995, ASME Paper No. 95-GT-14.
- [13] Schmidt, D. L., Sen, B., and Bogard, D. G., 1996, "Effects of Surface Roughness on Film Cooling," Proceedings of the ASME Turbo Expo, Birmingham, UK, June 10–13, 1996, ASME Paper No. 96-GT-299.
- [14] Bogard, D. G., Schmidt, D. L., and Tabbita, M., 1998, "Characterization and Laboratory Simulation of Turbine Airfoil Surface Roughness and Associated Heat Transfer," *ASME J. Turbomach.*, **120**(2), pp. 337–342.
- [15] Schmidt, D. L., and Bogard, D. G., 1996, "Effects of Free-Stream Turbulence and Surface Roughness on Film Cooling," Proceedings of the ASME Turbo Expo, Birmingham, UK, June 10–13, ASME Paper No. 96-GT-462.
- [16] Bons, J. P., MacArthur, C. D., and Rivir, R. B., 1994, "The Effect of High Freestream Turbulence on Film Cooling Effectiveness," *ASME J. Turbomach.*, **118**(4), pp. 814–825.
- [17] Kohli, A., and Bogard, D. G., 1997, "Effects of Very High Free-Stream Turbulence on the Jet-Mainstream Interaction in a Film Cooling Flow," *ASME J. Turbomach.*, **120**(4), pp. 785–790.
- [18] Wilkins, P. H., Lynch, S. P., Thole, K. A., Quach, S., Vincent, T., and Mongillo, D., 2022, "Effect of a Ceramic Matrix Composite Surface on Film Cooling," *ASME J. Turbomach.*, **144**(8), p. 081014.
- [19] Nemeth, N. N., Mital, S. K., and Lang, J., 2010, Evaluation of Solid Modeling Software for Finite Element Analysis of Woven Ceramic Matrix Composites, NASA/TM 2010-216250.
- [20] Eberly, M. K., and Thole, K. A., 2013, "Time-Resolved Film-Cooling Flows at High and Low Density Ratios," *ASME J. Turbomach.*, **136**(6), p. 061003.
- [21] Schroeder, R. P., and Thole, K. A., 2017, "Thermal Field Measurements for a Shaped Hole at Low and High Freestream Turbulence Intensity," *ASME J. Turbomach.*, **139**(2), p. 021012.
- [22] Schroeder, R. P., and Thole, K. A., 2017, "Effect of In-Hole Roughness on Film Cooling From a Shaped Hole," *ASME J. Turbomach.*, **139**(3), p. 031004.
- [23] Haydt, S., Lynch, S., and Lewis, S., 2017, "The Effect of a Meter-Diffuser Offset on Shaped Film Cooling Hole Adiabatic Effectiveness," *ASME J. Turbomach.*, **139**(9), p. 091012.
- [24] Haydt, S., Lynch, S., and Lewis, S., 2018, "The Effect of Area Ratio Change Via Increased Hole Length for Shaped Film Cooling Holes With Constant Expansion Angles," *ASME J. Turbomach.*, **140**(5), p. 051002.
- [25] Haydt, S., and Lynch, S., 2019, "Cooling Effectiveness for a Shaped Film Cooling Hole at a Range of Compound Angles," *ASME J. Turbomach.*, **141**(4), p. 041005.
- [26] Haydt, S., and Lynch, S., 2021, "Heat Transfer Coefficient Augmentation for a Shaped Film Cooling Hole at a Range of Compound Angles," *ASME J. Turbomach.*, **143**(5), p. 051012.
- [27] Robertson, D., 2004, "Roughness Impact on Turbine Vane Suction Side Film Cooling Effectiveness," Thesis, University of Texas.
- [28] Raffel, M., Willert, C. E., Scarano, F., Kahler, C. J., Wereley, S. T., and Kompenhans, J., 2018, *Particle Image Velocimetry A Practical Guide*, Springer International Publishing AG, Cham, Switzerland.
- [29] LaVision, 2020, "Product Manual for DaVis 10.1 Software," LaVision GmbH, Gottingen, Ger. Item No. 1105xxx.
- [30] Moffat, R. J., 1982, "Contributions to the Theory of Single-Sample Uncertainty Analysis," *J. Fluids Eng.*, **104**(2), pp. 2–258.
- [31] Figliola, R. S., and Beasley, D. E., 2011, *Theory and Design for Mechanical Measurements*, John Wiley & Sons, Inc, Hoboken, NJ.
- [32] Wieneke, B., 2015, "PIV Uncertainty Quantification From Correlation Statistics," *Meas. Sci. Technol.*, **26**(7), p. 074002.
- [33] Koutmos, P., and McGuirk, J. J., 1989, "Isothermal Flow in a Gas Turbine Combustor—A Benchmark Experimental Study," *Exp. Fluids*, **7**(5), pp. 344–354.